

Visualization of Thomas-Wigner rotations

G. Beyerle

Caputh, Germany

E-mail: mail@gbeyerle.de

Abstract. It is well known that a sequence of two non-collinear pure Lorentz transformations (boosts) is not a boost again, but involves a spatial rotation, the Wigner or Thomas-Wigner rotation. The formation of this rotation is visually illustrated by moving a Born-rigid object on a closed trajectory in several sections. Within each section the boost's proper time duration is assumed to be the same and the object's centre accelerates uniformly. Born-rigidity implies that the stern of this object accelerates faster than its bow. It is shown that at least five boosts are required to return the object's centre to its start position. With these assumptions, the Thomas-Wigner rotation angle depends on a single parameter only, the maximum speed reached within each boost section. The visualization highlights the close relationship between the Thomas-Wigner rotation and the relativity of simultaneity. Furthermore, it is illustrated that accelerated motion implies the formation of an event horizon. The event horizons associated with the five boosts constitute a boundary to the rotated Born-rigid object and ensure its finite size.

1. Introduction

In 1926 the British physicist Llewellyn Hilleth Thomas (1903–1992) resolved a discrepancy between observed line splittings of atomic spectra in an external magnetic field (Zeeman effect) and theoretical calculations at that time [see e.g. Tomonaga, 1997]. Thomas’ analysis [Thomas, 1926, 1927] explains the observed deviations in terms of a special relativistic effect [Einstein, 1905]. He recognized that a sequence of two non-collinear pure Lorentz transformations (boosts) cannot be expressed as one single boost. Rather, two non-collinear boosts correspond to a pure Lorentz transformation combined with a spatial rotation. This spatial rotation is known as Wigner rotation or Thomas-Wigner rotation, the corresponding rotation angle is the Thomas-Wigner angle [see e.g. Wigner, 1939; Ben-Menahem, 1985; Costella et al., 2001; Cushing, 1967; Ferraro and Thibeault, 1999; Fisher, 1972; Gelman, 1990; Kennedy, 2002; Mocanu, 1992; Rhodes and Semon, 2004; Rowe, 1984; Ungar, 1989, 1997; Gourgoulhon, 2013; Misner et al., 1973; Rębilas, 2015; Steane, 2012, and references therein].

The prevalent approach to visualize Thomas-Wigner rotations employs passive Lorentz transformations. An object \mathcal{G} is simultaneously observed from two inertial reference frames, [1] and [N], and \mathcal{G} is assumed to be at rest in both of them. Frame [N] is related to [1] by $N - 1$ pure Lorentz transformations

$$[1] \rightarrow [2] \rightarrow [3] \rightarrow \dots \rightarrow [N] \quad .$$

As already mentioned, non-zero Thomas-Wigner rotations require two non-collinear boosts. For given non-collinear boosts $[1] \rightarrow [2]$ and $[2] \rightarrow [3]$ there exists a unique third boost $[3] \rightarrow [4]$, such that \mathcal{G} is at rest with respect to both, frame [1] and frame [4]. Thus, non-zero Thomas-Wigner rotations imply $N \geq 4$. In the following frame [1] is taken to be the laboratory frame.

Following Jonsson [2007] in the present paper an alternative route to visualize Thomas-Wigner rotations using active or “physical” boosts is attempted. That is, \mathcal{G} is accelerated starting from and ending at zero velocity in the laboratory frame (frame [1]). During its journey \mathcal{G} performs several acceleration and/or deceleration manoeuvres. I suppose, that the mathematical complications created by using active boosts are outweighed by the visual impressions of \mathcal{G} moving through the series of acceleration phases and finally coming to rest in a rotated orientation (see fig. 5 below).

The paper is sectioned as follows. First, the approach is described in general terms and the basic assumptions are introduced. Second, uniform accelerations of Born-rigid objects are recalled. In the following section sequences of uniform, non-collinear accelerations for a given reference point and the motions of its adjacent grid vertices are calculated. The last two sections present the visualization results and discuss their implications. Details of the computer algebraic calculations performed in this study are given in Appendix A.

For simplicity length units of light-seconds, abbreviated “ls” (roughly 300,000 km) are being used; in these units the velocity of light is 1 ls/s.

2. Method

We consider the trajectory of a square-shaped grid \mathcal{G} . The grid consists of M vertices and is assumed to be Born-rigid, i.e. the distances between all grid points, as observed in the instantaneous comoving inertial frame, also known as the momentarily comoving inertial frame, remain constant [Born, 1909]. \mathcal{G} 's central point R serves as the reference point. R is uniformly accelerated for a predefined proper time period. To obtain a closed trajectory several of these sections with constant proper acceleration, but different boost direction are joined together.

In R 's instantaneous comoving frame the directions and magnitudes of the vertices' proper accelerations $\vec{\alpha}_i$ ($i = 1, \dots, M$) change simultaneously and discontinuously at the switchover from one boost to the next. The subscript i indicates that these accelerations are in general not the same for all vertex points. In reference frames other than the instantaneous comoving frame, the accelerations $\vec{\alpha}_i$ change asynchronously and \mathcal{G} , despite its Born-rigidity, appears distorted and twisted (see figure 5 below). On the other hand, \mathcal{G} 's Born-rigidity implies that the motion of the reference point R determines the trajectories of all remaining $M - 1$ vertices; it is sufficient to calculate R 's trajectory [Herglotz, 1909; Noether, 1910]. We note that the separations between individual switchover events are spacelike. I.e. the switchover events are causally disconnected and each vertex has to be “programmed” in advance to perform the required acceleration changes.

In the following, α_R and $\Delta\tau_R$ denote the magnitude of the proper acceleration of \mathcal{G} 's reference point R and the boost duration in terms of R 's proper time, respectively. To simplify the calculations we impose the following four conditions on all N boosts.

- (i) The grid \mathcal{G} is Born-rigid.
- (ii) At the start and after completion of the N th boost \mathcal{G} is at rest in frame [1]; R returns to its start position in frame [1].
- (iii) R 's proper acceleration α_R and the boost's proper duration $\Delta\tau_R$ are the same in all N sections.
- (iv) All boost directions and therefore all trajectories lie within the xy -plane.

Let the unit vector \hat{e}_1 denote the direction of the first boost in frame [1]. This first boost lasts for a proper time $\Delta\tau_R$, as measured by R 's clock, when R attains the final velocity $v_R \equiv \beta$ with respect to frame [1]. Frame [2] is now defined as R 's comoving inertial frame at this instant of time. The corresponding Lorentz matrix transforming a four-vector from frame [2] to frame [1] is

$$\Lambda(\gamma, \hat{e}_1) \equiv \begin{pmatrix} \gamma, & \gamma\beta\hat{e}_1^T \\ \gamma\beta\hat{e}_1, & \mathbf{1}_{3\times 3} + (\gamma - 1)\hat{e}_1 \cdot \hat{e}_1^T \end{pmatrix}. \quad (1)$$

Here, $\mathbf{1}_{3\times 3}$ is the 3×3 unit matrix, the superscript T denotes transposition, the Lorentz

factor is

$$\gamma \equiv \frac{1}{\sqrt{1 - \beta^2}} \quad (2)$$

and, in turn, $\beta = \sqrt{\gamma^2 - 1}/\gamma$. Similarly, frame [3] is R 's comoving inertial frame at the end of the second boost, etc. In general, the Lorentz transformation from frame [i] to frame [$i + 1$] is given by eqn. 1, with \hat{e}_1 replaced by \hat{e}_i , the direction of the i th boost in frame [i].

Assumption [iii] implies that the sole unknowns, which need to be determined, are the angles between consecutive boosts,

$$\zeta_{i,i+1} \equiv \arccos(\hat{e}_i^T \cdot \hat{e}_{i+1}) \quad . \quad (3)$$

The proper acceleration α_R and boost duration $\Delta\tau_R$ are taken to be given parameters. In the following the boost angles ζ will be replaced by the ‘‘half-angle’’ parametrization

$$T \equiv \tan\left(\frac{\zeta}{2}\right) \quad . \quad (4)$$

Eqn. 4 allows us to write expressions involving $\sin(\zeta)$ and $\cos(\zeta)$ as polynomials in T since

$$\begin{aligned} \sin(\zeta) &= \frac{2T}{1 + T^2} \\ \cos(\zeta) &= \frac{1 - T^2}{1 + T^2} \quad . \end{aligned} \quad (5)$$

We will find that a) no solutions exist if the number of boosts N is four or less, b) for $N = 5$ the solution is unique and c) the derived boost angles ζ depend solely on the selected value of $\gamma = 1/\sqrt{1 - \beta^2}$. Changing α_R and/or $\Delta\tau_R$ only affects the spatial and temporal scale of R 's trajectory (see below).

In section 4 it is shown that at least $N = 5$ boost are necessary, in order to satisfy assumptions [i], [ii], [iii] and [iv]. The derivations of $\zeta_{i,i+1} = \zeta_{i,i+1}(\gamma)$ are simplified by noting that the constraints [ii], [iii] and [iv] imply time reversal invariance. I.e. R 's trajectory from destination to start followed backward in time is a valid solution as well and therefore $\zeta_{i,i+1} = \zeta_{N-i,N-i+1}$ for $i = 1, \dots, N - 1$. Thus, for $N = 5$ the number of unknown reduces from four to two, $\zeta_{1,2} = \zeta_{4,5}$ and $\zeta_{2,3} = \zeta_{3,4}$.

3. Uniform acceleration of a Born-rigid object

Consider the uniform acceleration of the reference point R . We assume, the acceleration phase lasts for the proper time period $\Delta\tau_R$. During $\Delta\tau_R$ the reference point moves from location $\vec{r}_R(0)$ to location

$$\vec{r}_R(\Delta\tau_R) = \vec{r}_R(0) + \frac{1}{\alpha_R} (\cosh(\alpha_R \Delta\tau_R) - 1) \hat{e}_B \quad (6)$$

in the laboratory frame with unit vector \hat{e}_B denoting the boost direction [see e.g. Hamilton, 1978; Hobson et al., 2006; Misner et al., 1973; Rindler, 2006; Steane, 2012;

Styer, 2007]. The coordinate time duration Δt_R corresponding to the proper time duration $\Delta\tau_R$ is

$$\Delta t_R = \frac{1}{\alpha_R} \sinh(\alpha_R \Delta\tau_R) \quad (7)$$

and R 's final speed in the laboratory frame is

$$v_R = \tanh(\alpha_R \Delta\tau_R) = \beta \quad . \quad (8)$$

Let G be another vertex point of the grid \mathcal{G} at location $\vec{r}_G(0)$ and

$$b \equiv (\vec{r}_G(0) - \vec{r}_R(0)) \cdot \hat{e}_B \quad (9)$$

the projection of distance vector from R to G onto the boost direction \hat{e}_B . In the laboratory frame the vertices G and R start to accelerate simultaneously since \mathcal{G} is Born-rigid and analogous to eqns. 6, 7 and 8 we obtain for G 's trajectory

$$\begin{aligned} \vec{r}_G(\Delta\tau_G) &= \vec{r}_G(0) + \left(\frac{1}{\alpha_G} (\cosh(\alpha_G \Delta\tau_G) - 1) + b \right) \hat{e}_B \\ \Delta t_G &= \frac{1}{\alpha_G} \sinh(\alpha_G \Delta\tau_G) \\ v_G &= \tanh(\alpha_G \Delta\tau_G) \quad . \end{aligned} \quad (10)$$

We note, that the boost phase ends simultaneously for all grid points in R 's instantaneous comoving frame. Since \mathcal{G} is Born-rigid (assumption [i]), their speeds at the end of the boost phase have to be identical; in particular, $v_G = v_R$ and thus

$$\alpha_G \Delta\tau_G = \alpha_R \Delta\tau_R \quad . \quad (11)$$

Furthermore, \mathcal{G} 's Born-rigidity implies that the spatial distance between G and R in R 's comoving rest frame at the end of the boost phase is the same as the distance at the beginning. A brief calculation leads to

$$-\frac{1}{\alpha_G} (\gamma - 1) + b\gamma + \frac{1}{\alpha_R} (\gamma - 1) = b \quad (12)$$

which simplifies to

$$\alpha_G = \frac{1}{1 + b\alpha_R} \alpha_R \quad (13)$$

and with eqn. 11

$$\Delta\tau_G = (1 + b\alpha_R) \Delta\tau_R \quad . \quad (14)$$

Eqn. 13 expresses the well-known fact that the proper accelerations aboard a Born-rigid grid may differ from one vertex to the next. More specifically, at a location trailing the reference point R the acceleration exceeds α_R , vertex points leading R accelerate less than α_R . (In relativistic space travel the passengers in the bow of the spaceship suffer lower acceleration forces than those seated in the stern. This amenity of a more comfortable acceleration, however, is counterbalanced by faster ageing of the space passengers (eqn. 14). Here it is assumed, that relativistic spaceships are Born-rigidly constructed.)

This position-dependent acceleration is well-known from the Dewan-Beran-Bell spaceship paradox [Dewan and Beran, 1959; Dewan, 1963] and [Bell, 2004, chapter 9]. Two spaceships, connected by a Born-rigid wire, accelerate along the direction separating the two. According to eqn. 13 the trailing ship has to accelerate faster than the leading one. Conversely, if both accelerated at the same rate in the laboratory frame, Born-rigidity could not be maintained and the wire connecting the two ships would eventually break. This well-known, but admittedly counterintuitive fact is not a paradox in the true sense of the word as discussed extensively in the relevant literature [see e.g. Evett and Wangsness, 1960; Evett, 1972; Fernflores, 2011; Tartaglia and Ruggiero, 2003; Redžić, 2008; Franklin, 2010].

Eqns. 13 and 14 also imply, that $\alpha_G \rightarrow \infty$ and $\Delta\tau_G \rightarrow 0$, as the distance between a (trailing) vertex G and the reference point R approaches the critical value

$$b^* \equiv -1/\alpha_R \quad . \quad (15)$$

Clearly, the object \mathcal{G} cannot extend beyond this boundary, which in the following is referred to as “event horizon”. In section 6.2 we will discuss its consequences.

Finally, we note that eqn. 14 implies that a set of initially synchronized clocks mounted on a Born-rigid grid will in general fall out of synchronization once the grid is accelerated. Thus, the switchover events, which occur simultaneous in R ’s instantaneous comoving frame, are not simultaneous with respect to the time displayed by the vertex clocks. Since switchover events are causally not connected and lie outside of each others’ lightcone, the acceleration changes have to be “programmed” into each vertex in advance [Eriksen et al., 1982].

4. Sequence of uniform accelerations

In the previous section R ’s trajectory throughout a specific acceleration phase (eqn. 10) was discussed. Now several of these segments are linked together to form a closed trajectory for R . Let $A^{[k]}$ denote R ’s start event as observed in frame $[k]$ and $B^{[k]}$, $C^{[k]}$, etc. correspondingly denote the “switchover” events between 1st and 2st boost, 2nd and 3rd boost, etc., respectively. The bracketed superscripts indicate the reference frame. Frame [1], i.e. $k = 1$, is the laboratory frame, frame [2] is obtained from frame [1] using Lorentz transformation $\Lambda(\gamma, -\hat{e}_1)$ (eqn. 1). Generally, frame $[k + 1]$ is calculated from frame $[k]$ using the transformation matrix $\Lambda(\gamma, -\hat{e}_k)$.

First, we determine the smallest number of boosts that satisfies the four assumptions listed in section 2. Denoting the number of boosts by N , it is self-evident that $N \geq 3$, since for $N = 1$ the requirement of vanishing final velocity cannot be met if $v_R \neq 0$. And for $N = 2$ the requirement of vanishing final velocity implies collinear boost directions. With two collinear boosts, however, the reference point R does not move along a closed trajectory. In addition, we note, that collinear boosts imply vanishing Thomas-Wigner rotation [see e.g. Steane, 2012].

4.1. Three boosts

Consider three boosts of the reference point R starting from location A and returning to location D via locations B and C. In the laboratory frame (frame [1]) the four-position at the destination D is given by

$$\begin{aligned} \mathbf{P}_D^{[1]} &= \mathbf{P}_A^{[1]} + \mathbf{S}_{A \rightarrow B}^{[1]} \\ &\quad + \Lambda(\gamma, -\hat{e}_1) \cdot \mathbf{S}_{B \rightarrow C}^{[2]} \\ &\quad + \Lambda(\gamma, -\hat{e}_1) \cdot \Lambda(\gamma, -\hat{e}_2) \cdot \mathbf{S}_{C \rightarrow D}^{[3]} \end{aligned} \quad (16)$$

and

$$\mathbf{V}_D^{[1]} = \Lambda(\gamma, -\hat{e}_1) \cdot \Lambda(\gamma, -\hat{e}_2) \cdot \Lambda(\gamma, -\hat{e}_3) \cdot \mathbf{V}_D^{[4]} \quad (17)$$

is the corresponding four-velocity. Here, the four-vector

$$\begin{aligned} \mathbf{S}_{A \rightarrow B}^{[1]} &\equiv \frac{1}{\alpha_R} \begin{pmatrix} \sinh(\alpha_R \Delta\tau_R) \\ (\cosh(\alpha_R \Delta\tau_R) - 1) \hat{e}_1 \end{pmatrix} \\ &= \frac{1}{\alpha_R} \begin{pmatrix} \gamma \beta \\ (\gamma - 1) \hat{e}_1 \end{pmatrix} \end{aligned} \quad (18)$$

describes R 's trajectory in spacetime from A to B (eqn. 10). $\mathbf{S}_{B \rightarrow C}^{[2]}$ and $\mathbf{S}_{C \rightarrow D}^{[3]}$ are defined correspondingly. Assumption [ii] implies that

$$\vec{P}_A^{[1]} = \vec{P}_D^{[1]} = \vec{P}_A^{[4]} = \vec{P}_D^{[4]} = \vec{0} \quad (19)$$

and

$$\mathbf{V}_A^{[1]} = \mathbf{V}_D^{[1]} = \mathbf{V}_A^{[4]} = \mathbf{V}_D^{[4]} = \begin{pmatrix} 1 \\ \vec{0} \end{pmatrix} . \quad (20)$$

Inserting eqn. 1 into eqn. 17 yields

$$T_{12} = T_{23} = \pm \sqrt{2\gamma + 1} \quad (21)$$

(see Appendix A) and, in turn, using eqn. 19 we obtain

$$\vec{P}_D^{[1]} = \frac{1}{(\gamma + 1)^2} \begin{pmatrix} -(\gamma - 1)^2 (2\gamma + 1)^2 \\ -(\gamma - 1) (2\gamma + 1)^{\frac{3}{2}} (3\gamma + 1) \\ 0 \end{pmatrix} \stackrel{!}{=} \vec{0} . \quad (22)$$

Its only solution for real-valued β is the trivial solution $\gamma = 1$, i.e. $\beta = 0$. Thus, there are no non-trivial solutions for $N = 3$ boosts, which are consistent with the assumptions [i] to [iv].

4.2. Four boosts

For a sequence of four boosts time reversal symmetry implies that R 's velocity in the laboratory frame vanishes at event C after the second boost, i.e. $\vec{V}_C^{[1]} = \vec{0}$. However, stationarity in the laboratory frame can only be achieved if the first two boosts $A \rightarrow B$ and $B \rightarrow C$ are collinear. In order to fulfil assumption [ii] the third and fourth boosts

have to be collinear with the first (and second) boost as well. As already noted, a sequence of collinear boosts, however, does not produce a non-zero Thomas-Wigner rotation.

4.3. Five boosts

For a sequence of five boosts, i.e. $N = 5$, the expressions for four-position and four-velocity are

$$\begin{aligned}
 \mathbf{P}_F^{[1]} &= \mathbf{P}_A^{[1]} + \mathbf{S}_{A \rightarrow B}^{[1]} & (23) \\
 &+ \Lambda(\gamma, -\hat{e}_1) \cdot \mathbf{S}_{B \rightarrow C}^{[2]} \\
 &+ \Lambda(\gamma, -\hat{e}_1) \cdot \Lambda(\gamma, -\hat{e}_2) \cdot \mathbf{S}_{C \rightarrow D}^{[3]} \\
 &+ \Lambda(\gamma, -\hat{e}_1) \cdot \Lambda(\gamma, -\hat{e}_2) \cdot \Lambda(\gamma, -\hat{e}_3) \cdot \mathbf{S}_{D \rightarrow E}^{[4]} \\
 &+ \Lambda(\gamma, -\hat{e}_1) \cdot \Lambda(\gamma, -\hat{e}_2) \cdot \Lambda(\gamma, -\hat{e}_3) \cdot \Lambda(\gamma, -\hat{e}_4) \cdot \mathbf{S}_{E \rightarrow F}^{[5]}
 \end{aligned}$$

and

$$\begin{aligned}
 \mathbf{V}_F^{[1]} &= \Lambda(\gamma, -\hat{e}_1) \cdot \Lambda(\gamma, -\hat{e}_2) \cdot \Lambda(\gamma, -\hat{e}_3) & (24) \\
 &\cdot \Lambda(\gamma, -\hat{e}_4) \cdot \Lambda(\gamma, -\hat{e}_5) \cdot \mathbf{V}_F^{[6]} \quad ,
 \end{aligned}$$

respectively. Analogous to eqns. 19 and 20 assumption [ii] implies that

$$\vec{P}_A^{[1]} = \vec{P}_F^{[1]} = \vec{P}_A^{[6]} = \vec{P}_F^{[6]} = \vec{0} \quad (25)$$

and

$$\mathbf{V}_A^{[1]} = \mathbf{V}_F^{[1]} = \mathbf{V}_A^{[6]} = \mathbf{V}_F^{[6]} = \begin{pmatrix} 1 \\ \vec{0} \end{pmatrix} \quad . \quad (26)$$

To simplify the expressions in eqns. 23 and 24 time reversal symmetry is invoked again. It implies that the set of boost vectors $-\hat{e}_5, -\hat{e}_4, \dots, -\hat{e}_1$ constitutes a valid solution, provided $\hat{e}_1, \hat{e}_2, \dots, \hat{e}_5$ is one and satisfies assumptions [i] to [iv]. Thereby the number of unknown is reduced from four to two, the angle between the boost vectors \hat{e}_1 and \hat{e}_2 , and the angle between \hat{e}_2 and \hat{e}_3

$$\begin{aligned}
 \zeta_{1,2} &\equiv \arccos(\hat{e}_1^T \cdot \hat{e}_2) = \arccos(\hat{e}_4^T \cdot \hat{e}_5) & (27) \\
 \zeta_{2,3} &\equiv \arccos(\hat{e}_2^T \cdot \hat{e}_3) = \arccos(\hat{e}_3^T \cdot \hat{e}_4) \quad .
 \end{aligned}$$

Fig. 3 illustrates the sequence of the five boosts in the laboratory frame (frame [1]). R moves along a closed trajectory starting at location A and returning to F via B, C, D and E. Since the start and final velocities are zero, the motion between A and B and, likewise, between E and F is rectilinear. In contrast, the trajectory connecting B and E (via C and D) appears curved in frame [1]. As discussed and illustrated below the curved paths appear as straight lines in the corresponding frame (see fig.4).

From eqns. 24 and 26 it follows that

$$((T_{12})^2 - 2\gamma - 1)(T_{23})^2 - 4(1 + \gamma)T_{12}T_{23} + (T_{12})^2 + 4\gamma^2 + 2\gamma - 1 = 0 \quad (28)$$

with the two unknowns T_{12} and T_{23} (for details see Appendix A). Eqn. 28 has the two solutions

$$T_{23}^{(\pm)} = \frac{1}{-(T_{12})^2 + 2\gamma + 1} \times \left(-2T_{12}(\gamma + 1) \pm \sqrt{-(T_{12})^4 + 8(T_{12})^2\gamma + 6(T_{12})^2 + 8\gamma^3 + 8\gamma^2 - 1} \right) \quad (29)$$

provided

$$(T_{12})^2 - 2\gamma - 1 \neq 0 \quad . \quad (30)$$

Assumption [ii] implies that $\vec{P}_F^{[1]} = 0$, i.e. the spatial component of the event $\mathbf{P}_F^{[1]}$ vanishes. Since all motions are restricted to the xy -plane, it suffices to consider the x - and y -components of eqn. 25. The y -component leads to the equations (see Appendix A)

$$\begin{aligned} & (T_{12})^8 \\ & + (T_{12})^6 4(\gamma + 2) \\ & + (T_{12})^4 (-2)(2\gamma + 1)(2\gamma^2 + 8\gamma + 9) \\ & + (T_{12})^2 (-4)(8\gamma^4 + 28\gamma^3 + 26\gamma^2 + 5\gamma - 2) \\ & - (2\gamma + 1)^3 (4\gamma^2 + 2\gamma - 1) \\ & = 0 \end{aligned} \quad (31)$$

or

$$\begin{aligned} & (T_{12})^8 (\gamma^2 + 6\gamma + 9) \\ & + (T_{12})^6 (-4)(6\gamma^3 - 15\gamma^2 - 12\gamma + 5) \\ & + (T_{12})^4 (-2)(24\gamma^4 - 44\gamma^3 - 55\gamma^2 + 26\gamma + 1) \\ & + (T_{12})^2 (-4)(8\gamma^5 - 16\gamma^4 - 14\gamma^3 + 5\gamma^2 + 1) \\ & + (4\gamma^2 + \gamma - 1)^2 \\ & = 0 \quad . \end{aligned} \quad (32)$$

For $\gamma = 1$ eqn. 32 yields

$$(T_{12})^8 + 4(T_{12})^6 + 6(T_{12})^4 + 4(T_{12})^2 + 1 = 0 \quad (33)$$

which has no real-valued solution for T_{12} .

It turns out (see Appendix A) that equating the x -component of $\vec{P}_F^{[1]} = 0$ to zero, results in an expression containing two factors as well, one of which is identical to the LHS of eqn. 31. Thus, eqn. 31 satisfies the condition $\vec{P}_F^{[1]} = 0$.

Eqn. 31 is a polynomial equation of degree four in terms of $(T_{12})^2$. Its solutions are classified according to the value of the discriminant Δ , which for eqn. 31 evaluates to (see e.g. en.wikipedia.org/wiki/Quartic_function)

$$\begin{aligned} \Delta = & -524288\gamma(\gamma - 1)^3(\gamma + 1)^7 \\ & \times (4\gamma^4 + 28\gamma^3 + 193\gamma^2 + 234\gamma + 81) \quad . \end{aligned} \quad (34)$$

For non-trivial boost $\gamma > 1$, the discriminant is negative and therefore the roots of the quartic polynomial consist of two pairs of real and complex conjugate numbers. The real-valued solutions are

$$(T_{12})^2 = -(\gamma + 2) + \mathcal{S} + \frac{1}{2} \sqrt{-4\mathcal{S}^2 - 2p - \frac{q}{\mathcal{S}}} \quad (35)$$

and

$$\left(T_{12}^{(b)}\right)^2 = -(\gamma + 2) + \mathcal{S} - \frac{1}{2} \sqrt{-4\mathcal{S}^2 - 2p - \frac{q}{\mathcal{S}}} \quad (36)$$

with

$$\begin{aligned} p &\equiv -2(\gamma + 1)(4\gamma^2 + 17\gamma + 21) \\ q &\equiv -16(\gamma + 1)(\gamma^2 - 2\gamma - 9) \\ \mathcal{S} &\equiv \frac{1}{2\sqrt{3}} \sqrt{-2p + \mathcal{Q} + \frac{\Delta_0}{\mathcal{Q}}} \\ \Delta_0 &\equiv 16(\gamma + 1)^2(4\gamma^4 + 28\gamma^3 + 157\gamma^2 + 126\gamma + 9) \\ \mathcal{Q} &\equiv 4\sqrt[3]{\mathcal{Q}_0 + 12\sqrt{6}\sqrt{\mathcal{Q}_0}} \\ \mathcal{Q}_0 &\equiv \gamma(\gamma - 1)^3(\gamma + 1)^7(4\gamma^4 + 28\gamma^3 + 193\gamma^2 + 234\gamma + 81) \end{aligned} \quad (37)$$

The solution listed in eqn. 36 turns out to be negative and thus does not produce a real-valued solution for T_{12} . The remaining two solutions of eqn. 31

$$\begin{aligned} \left(T_{12}^{(c)}\right)^2 &= -(\gamma + 2) - \mathcal{S} + \frac{1}{2} \sqrt{-4\mathcal{S}^2 - 2p + \frac{q}{\mathcal{S}}} \\ \left(T_{12}^{(d)}\right)^2 &= -(\gamma + 2) - \mathcal{S} - \frac{1}{2} \sqrt{-4\mathcal{S}^2 - 2p + \frac{q}{\mathcal{S}}} \end{aligned} \quad (38)$$

correspond to replacing $\mathcal{S} \rightarrow -\mathcal{S}$ in eqns. 35 and 36, are complex-valued and therefore disregarded as well.

The other unknown, T_{23} , follows from eqn. 29 by choosing the positive square root $+\sqrt{(T_{12})^2}$ and using

$$T_{23} \equiv T_{23}^{(+)} \quad (39)$$

(see eqn. 28). For a given Lorentz factor γ the angles between the boost directions \hat{e}_i and \hat{e}_{i+1} follow from

$$\begin{aligned} \zeta_{1,2}(\gamma) &= \arccos(\hat{e}_1^T \cdot \hat{e}_2) = 2 \arctan\left(+\sqrt{(T_{12}(\gamma))^2}\right) \\ \zeta_{2,3}(\gamma) &= \arccos(\hat{e}_2^T \cdot \hat{e}_3) = 2 \arctan\left(+\sqrt{(T_{23}(\gamma))^2}\right) \end{aligned} \quad (40)$$

and, with $\zeta_{4,5} = \zeta_{1,2}$ and $\zeta_{3,4} = \zeta_{2,3}$, the orientation of the five boost directions \hat{e}_i for $i = 1, \dots, 5$ within the xy -plane are obtained.

Fig. 1 shows numerical values of the boost angles $\zeta_{1,2}$ and $\zeta_{2,3}$ as a function of γ . The angles increase from

$$\zeta_{1,2}(\gamma = 1) = 2 \arctan\left(\sqrt{-5 + 4\sqrt{10}}\right) \approx 140.2^\circ$$

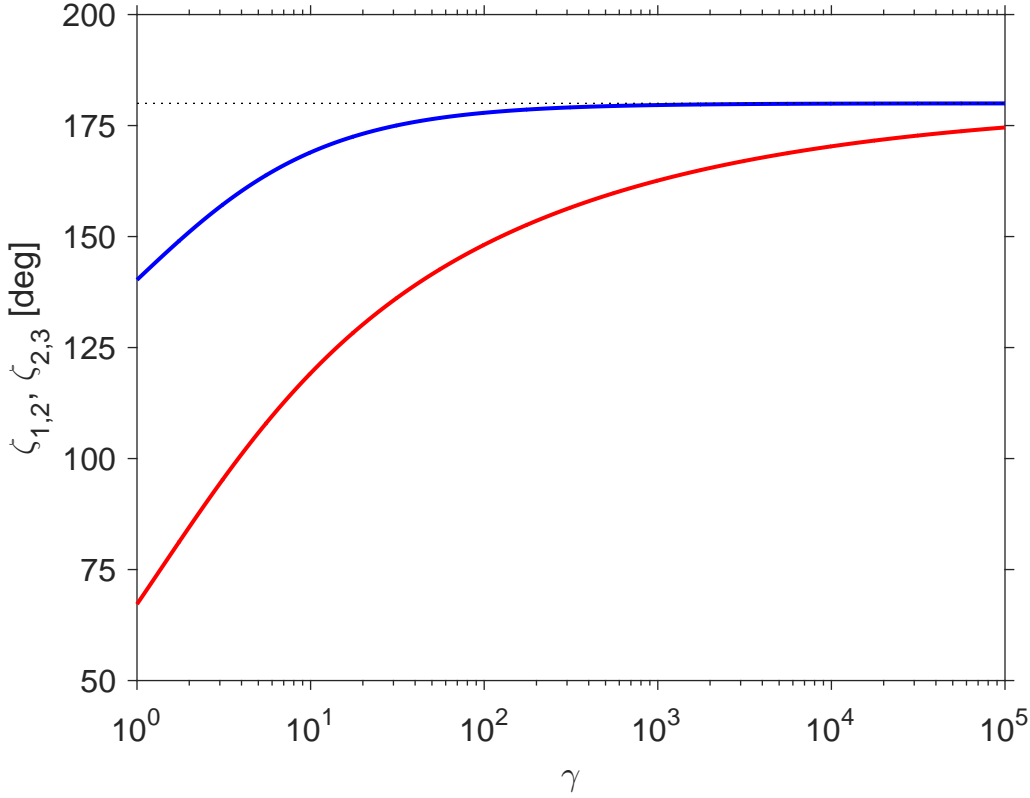


Figure 1. The angle between the boost direction vectors \hat{e}_1 and \hat{e}_2 in frame [1] (blue line), and the angle between \hat{e}_2 and \hat{e}_3 in frame [2] (red) as a function of γ . The dotted line marks $+180^\circ$, the limit of $\zeta_{1,2}$ and $\zeta_{2,3}$ for $\gamma \rightarrow \infty$.

and

$$\zeta_{2,3}(\gamma = 1) = 2 \arctan \left(\frac{\sqrt{-5 + 4\sqrt{10}} - \sqrt{3}\sqrt{-5 + 2\sqrt{10}}}{-2 + \sqrt{10}} \right) \approx 67.2^\circ$$

at $\gamma = 1$ to $\zeta_{1,2}(\gamma \rightarrow \infty) = +180^\circ = \zeta_{2,3}(\gamma \rightarrow \infty)$ as $\gamma \rightarrow \infty$.

Fig. 2 depicts the orientation of the five boost directions for several values of γ . For illustrative purposes the first boost vector \hat{e}_1 is taken to point along the x -axis. We note that the panels in fig. 2 do not represent a specific reference frame; rather, each vector \hat{e}_k is plotted with respect to frame $[k]$ ($k = 1, \dots, 5$). The four panels show the changes in boost directions for increasing values of γ . Interestingly, the asymptotic limits $\zeta_{1,2}(\gamma \rightarrow \infty) = +180^\circ$ and $\zeta_{2,3}(\gamma \rightarrow \infty) = +180^\circ$ imply that in the relativistic limit $\gamma \rightarrow \infty$ the trajectory of R essentially reduces to one-dimensional motions along the x -axis. At the same time the Thomas-Wigner rotation angle increases to $+360^\circ$ as $\gamma \rightarrow \infty$ (see the discussion in section 6 below).

Since the accelerated object is Born-rigid, the trajectories of all grid vertices G are uniquely determined once the trajectory of the reference point R is known [Herglotz, 1909; Noether, 1910; Eriksen et al., 1982]. Following the discussion in section 3 the position and coordinate time of a random vertex G , in the frame comoving with R

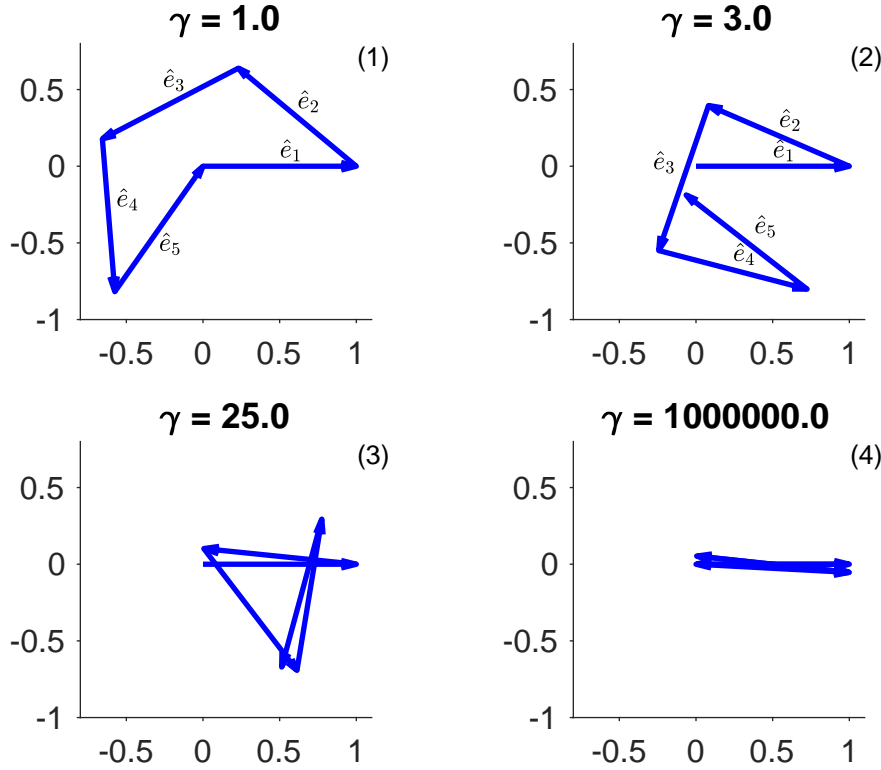


Figure 2. Boost directions for four different values of $\gamma = 1/\sqrt{1-\beta^2}$. \hat{e}_k is assumed to point along the x -axis. In the relativistic limit $\gamma \rightarrow \infty$ the angles between \hat{e}_k and \hat{e}_{k+1} approach $+180^\circ$ and the motion of the reference point R tends to be more and more restricted along the x -axis (see panel (4)), i.e. in the relativistic limit the object's trajectory transitions from a two- to a one-dimensional motion.

at the beginning of the corresponding acceleration phase, follows from eqns. 10. The resulting trajectories are discussed in the next section.

5. Visualization

The trajectory of the reference point R within the xy -plane for a boost velocity of $\beta = 1/2$, corresponding to $\gamma = 2/\sqrt{3} \approx 1.15$, is displayed in fig. 3. It is plotted in the laboratory frame (frame [1]) as black solid line. The same trajectory as it appears to an observer in frame [6] is marked in grey. The two frames are stationary with respect to other, but rotated by a Thomas-Wigner angle of about 14.4° . In addition, dots show the spatial component of the four switchover events B, C, D and E in the two frames. As required by assumption [ii] the start and final positions, corresponding to the events A and F, coincide.

Fig. 4 shows the same trajectory as fig. 3. In addition, R 's trajectories as recorded by observers in the frames [2], ..., [5] are plotted as well (solid coloured lines). Corresponding switchover events are connected by dashed lines. At $B^{[2]}$, $C^{[3]}$, $D^{[4]}$ and

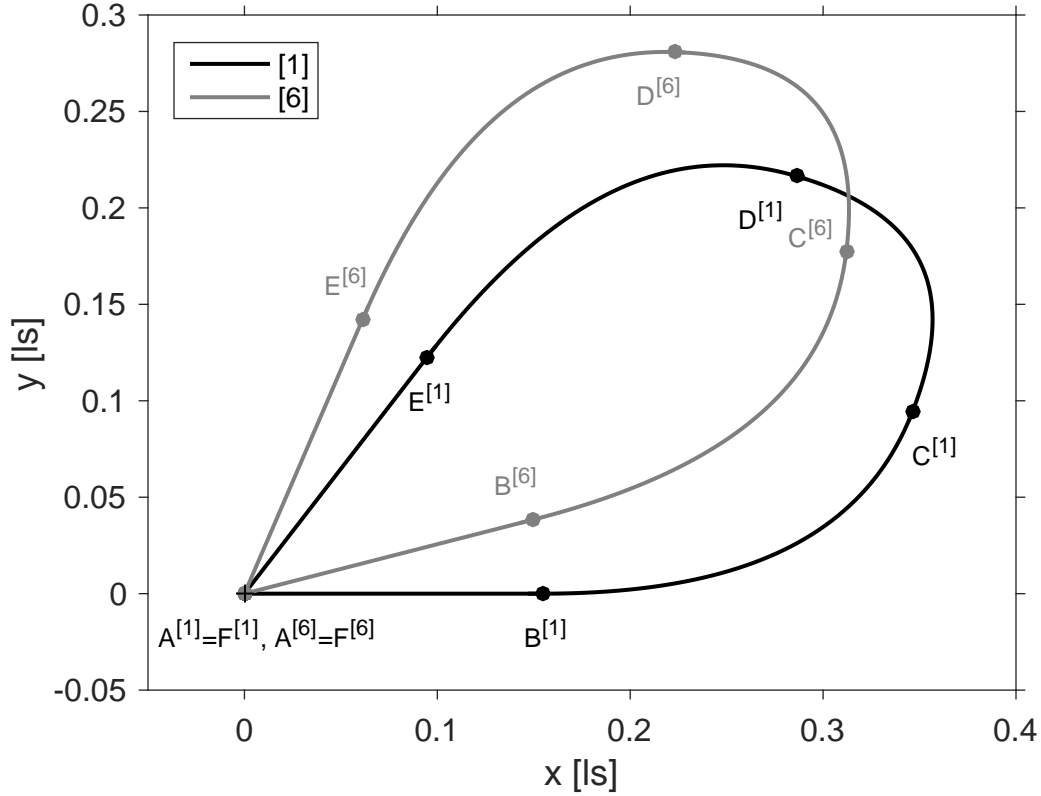


Figure 3. Trajectories of reference point R for $\gamma = 2/\sqrt{3} \approx 1.15$ as seen from reference frames [1] (laboratory frame) and [6]. The two frames are stationary with respect to each other, but rotated by a Thomas-Wigner angle of $\theta_{TW} = 14.4^\circ$.

$E^{[5]}$ (and of course at the start event $A^{[1,6]}$ and destination event $F^{[1,6]}$) the reference point R slows down and/or accelerates from zero velocity producing a kink in the trajectory. In all other cases the tangent vectors of the trajectories, i.e. the velocity vectors are continuous at the switchover points.

With eqns. 35 and 39 all necessary ingredients to visualize the relativistic motion of a Born-rigid object are available. In fig. 5 the object is modelled as a square-shaped grid of 11×11 points, arranged around the reference point R . The object uniformly accelerates in the xy -plane changing the boost directions by the four angles $\zeta_{1,2}$ (as measured in frame [2]), $\zeta_{2,3}$ (measured in frame [3]), $\zeta_{2,3}$ (measured in frame [4]) and finally $\zeta_{1,2}$ (measured in frame [5]). The vertices' colour code indicates the corresponding boost section. The 16 panels depict the grid positions in the laboratory frame (frame [1]) for specific values of coordinate time displayed in the top right.

To improve the visual impression the magnitude of the Thomas-Wigner rotation in fig. 5 is enlarged by increasing the boost velocity from $\beta = 0.5$ in figs. 3 and 4 to $\beta = 0.7$ corresponding to $\gamma \approx 1.4$. Despite appearance the grid \mathcal{G} is Born-rigid; in R 's comoving inertial frame the grid maintains its original square shape. In the laboratory frame, however, \mathcal{G} appears compressed, when it starts to accelerate or decelerate and sheared,

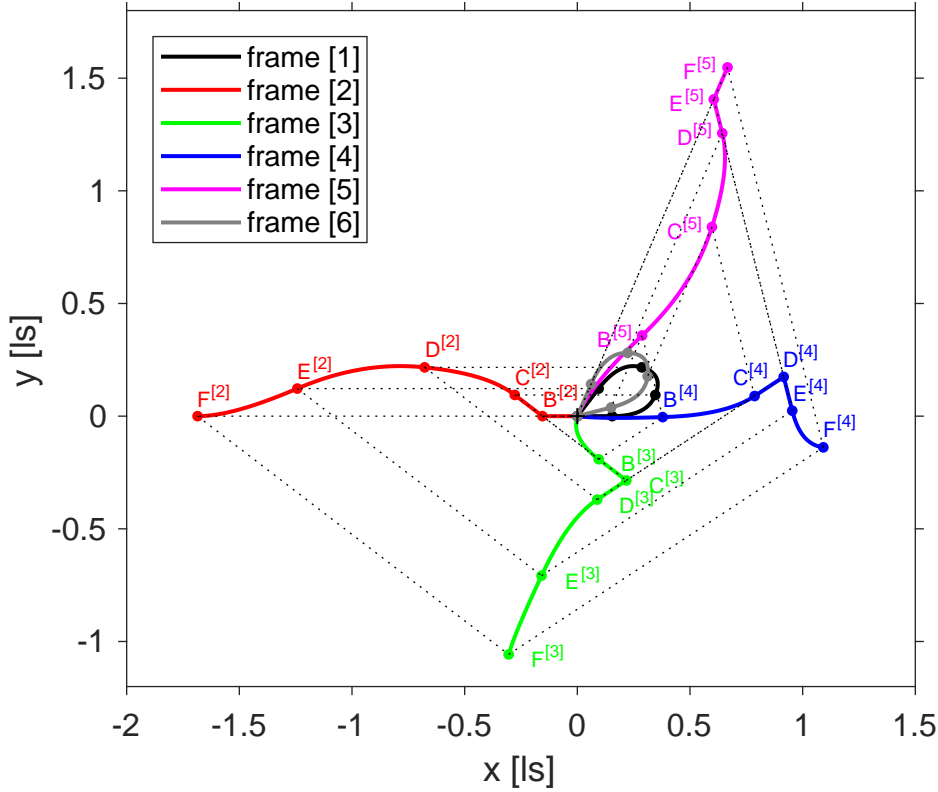


Figure 4. Trajectories of the reference point R as seen from the six reference frames [1], [2], ..., [6]. The switchover points are marked by $X_i^{[k]}$ with $X = A, \dots, F$. Corresponding switchover points are connected by dashed lines. The Lorentz factor is $\gamma = 2/\sqrt{3} \approx 1.15$.

when one part of \mathcal{G} has not yet finished boost k , but the remaining part of \mathcal{G} already has transitioned to the next boost section $k + 1$. This feature is clearly evident from panels (4), (7), (10) or (13) in fig. 5 with the occurrence of two colours indicating two boost sections taking effect at the same epoch of coordinate time. We note, however, that the switchover events occur simultaneously for all grid points in R 's comoving frame. The non-uniform colourings illustrate the asynchronism of the switchovers in the laboratory frame and thereby the relationship between Thomas-Wigner rotations and the non-existence of absolute simultaneity.

6. Discussion

In this final section the Thomas-Wigner rotation angle is calculated from the known boost angles $\zeta_{1,2}(\gamma)$ and $\zeta_{2,3}(\gamma)$ (eqn. 40). Second, the question of size limits of Born-rigid objects, Thomas-Wigner-rotated by a series of boosts, is addressed.

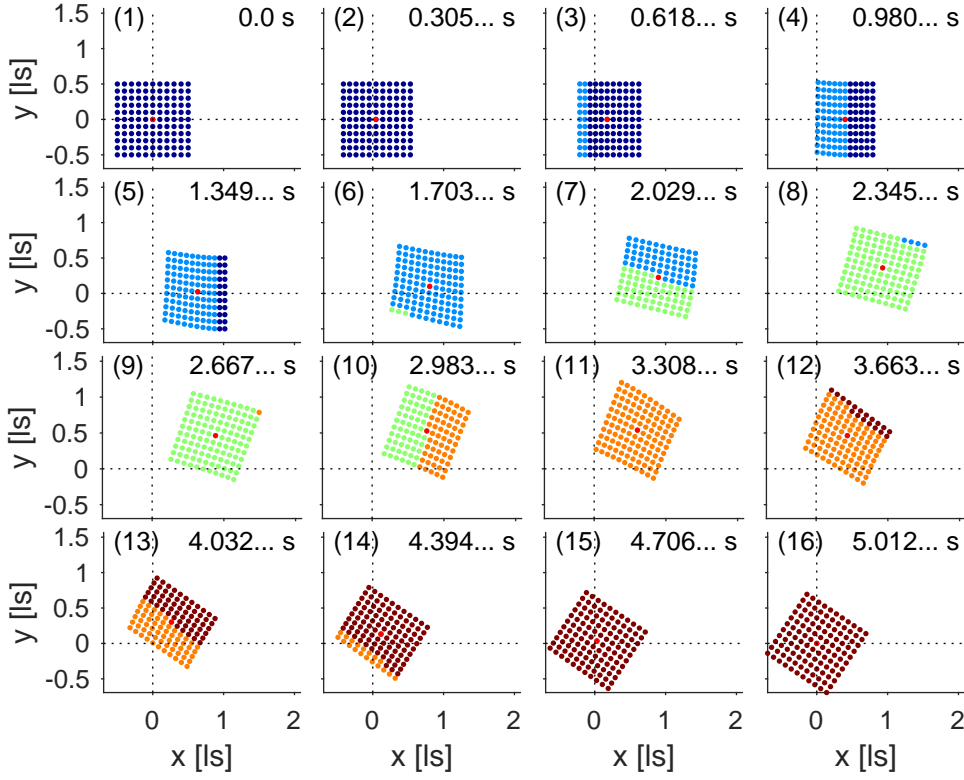


Figure 5. A series of grid positions as seen in the laboratory frame. The boost velocity is taken to be $\beta = 0.7$, the resulting Thomas-Wigner rotation angle amounts to about 33.7° . Coordinate time is displayed in the top right corner of each panel. The five boost phases are distinguished by colour. It is evident that switchovers between boosts do not occur simultaneously in the laboratory frame. The reference point (marked in red) moves along its trajectory counterclockwise, whereas the grid Thomas-Wigner rotates clockwise. For details see text.

6.1. Derivation of Thomas-Wigner angle

From the preceding sections follows a straightforward calculation of the Thomas-Wigner angle as a function of Lorentz factor γ . Assumption [ii] implies that the sequence of the five Lorentz transformations $[6] \rightarrow [5] \rightarrow \dots \rightarrow [1]$ is constructed such that frame [6] is stationary with respect to frame [1] and their spatial origins coincide. I.e. the combined transformation reduces to an exclusively spatial rotation and the corresponding Lorentz matrix can be written as

$$\begin{aligned}
 & \Lambda(\gamma, -\hat{e}_1) \cdot \Lambda(\gamma, -\hat{e}_2) \cdot \Lambda(\gamma, -\hat{e}_3) \cdot \Lambda(\gamma, -\hat{e}_4) \cdot \Lambda(\gamma, -\hat{e}_5) \\
 &= \begin{pmatrix} 1 & 0 & 0 & 0 \\ 0 & R_{1,1} & R_{1,2} & R_{1,3} \\ 0 & R_{2,1} & R_{2,2} & R_{2,3} \\ 0 & R_{3,1} & R_{3,2} & R_{3,3} \end{pmatrix}.
 \end{aligned} \tag{41}$$

Since the rotation is confined to the xy -plane, $R_{3,i} = 0 = R_{i,3}$ with $i = 1, 2, 3$. The remaining elements

$$\begin{aligned} R_{1,1}(\gamma) &= R_{2,2}(\gamma) \equiv \cos(\theta_{TW}(\gamma)) \\ R_{1,2}(\gamma) &= -R_{2,1}(\gamma) \equiv \sin(\theta_{TW}(\gamma)) \end{aligned} \quad (42)$$

yield the Thomas-Wigner rotation angle

$$\begin{aligned} \tilde{\theta}_{TW}(\gamma) &\equiv \text{atan2}(R_{2,1}(\gamma), R_{1,1}(\gamma)) \\ \theta_{TW}(\gamma) &\equiv \begin{cases} \tilde{\theta}_{TW}(\gamma) & : \tilde{\theta}_{TW}(\gamma) \geq 0 \\ \tilde{\theta}_{TW}(\gamma) + 2\pi & : \tilde{\theta}_{TW}(\gamma) < 0 \end{cases} \end{aligned} \quad (43)$$

with $\text{atan2}(\cdot, \cdot)$ denoting the four-quadrant inverse tangent. The definition of $\theta_{TW}(\gamma)$ in eqn. 43 ensures that angles exceeding $+180^\circ$ are unwrapped and mapped into the interval $[0^\circ, +360^\circ]$ (see fig. 6).

Using eqn. 41 the rotation matrix elements $R_{1,1}$ and $R_{2,1}$, expressed in terms of T_{12} and T_{23} (eqn. 4), are (see Appendix A)

$$\begin{aligned} R_{1,1}(\gamma) &= -1 + \frac{(\gamma + 1)}{((T_{12})^2 + 1)^4 ((T_{23})^2 + 1)^4} \\ &\times \left((T_{12})^4 (T_{23})^4 + 2 (T_{12})^4 (T_{23})^2 + (T_{12})^4 \right. \\ &- 4 (T_{12})^3 (T_{23})^3 \gamma + 4 (T_{12})^3 (T_{23})^3 - 4 (T_{12})^3 T_{23} \gamma \\ &+ 4 (T_{12})^3 T_{23} - 2 (T_{12})^2 (T_{23})^4 \gamma + 4 (T_{12})^2 (T_{23})^4 \\ &+ 4 (T_{12})^2 (T_{23})^2 \gamma^2 + 8 (T_{12})^2 (T_{23})^2 \gamma - 8 (T_{12})^2 (T_{23})^2 \\ &- 4 (T_{12})^2 \gamma^2 + 10 (T_{12})^2 \gamma - 4 (T_{12})^2 \\ &+ 12 T_{12} (T_{23})^3 \gamma - 12 T_{12} (T_{23})^3 - 16 T_{12} T_{23} \gamma^2 \\ &+ 12 T_{12} T_{23} \gamma + 4 T_{12} T_{23} + 2 (T_{23})^4 \gamma \\ &\left. - (T_{23})^4 - 4 (T_{23})^2 \gamma^2 + 6 (T_{23})^2 + 4 \gamma^2 - 2 \gamma - 1 \right)^2 \end{aligned} \quad (44)$$

and

$$\begin{aligned} R_{2,1}(\gamma) &= \frac{4(\gamma - 1)(\gamma + 1)}{((T_{12})^2 + 1)^4 ((T_{23})^2 + 1)^4} \\ &\times \left((T_{12})^3 (T_{23})^2 + (T_{12})^3 + 3 (T_{12})^2 (T_{23})^3 \right. \\ &- 2 (T_{12})^2 T_{23} \gamma + (T_{12})^2 T_{23} + T_{12} (T_{23})^4 \\ &- 2 T_{12} (T_{23})^2 \gamma - 3 T_{12} (T_{23})^2 + 2 T_{12} \gamma \\ &\left. - (T_{23})^3 + 2 T_{23} \gamma + T_{23} \right) \\ &\times \left((T_{12})^4 (T_{23})^4 + 2 (T_{12})^4 (T_{23})^2 + (T_{12})^4 \right. \\ &- 4 (T_{12})^3 (T_{23})^3 \gamma + 4 (T_{12})^3 (T_{23})^3 - 4 (T_{12})^3 T_{23} \gamma \\ &+ 4 (T_{12})^3 T_{23} - 2 (T_{12})^2 (T_{23})^4 \gamma + 4 (T_{12})^2 (T_{23})^4 \end{aligned} \quad (45)$$

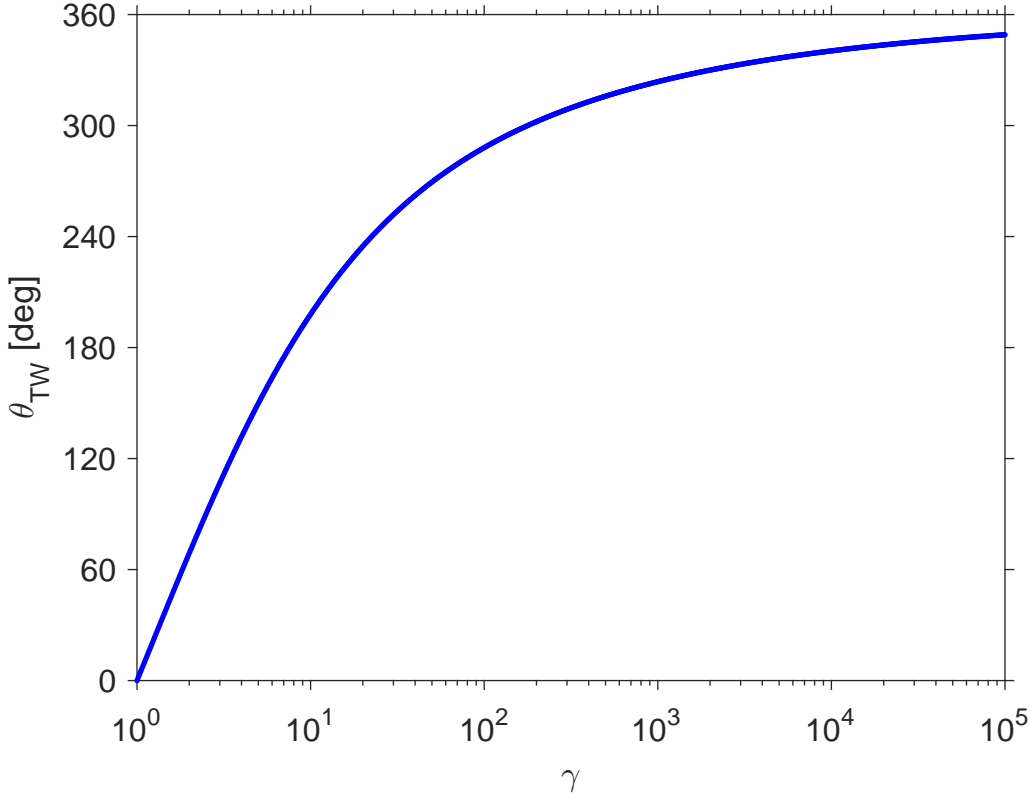


Figure 6. Thomas-Wigner rotation angle as a function of γ . For clarity the angle has been unwrapped to the range $[0^\circ, +360^\circ]$.

$$\begin{aligned}
& + 4 (T_{12})^2 (T_{23})^2 \gamma^2 + 8 (T_{12})^2 (T_{23})^2 \gamma - 8 (T_{12})^2 (T_{23})^2 \\
& - 4 (T_{12})^2 \gamma^2 + 10 (T_{12})^2 \gamma - 4 (T_{12})^2 \\
& + 12 T_{12} (T_{23})^3 \gamma - 12 T_{12} (T_{23})^3 - 16 T_{12} T_{23} \gamma^2 \\
& + 12 T_{12} T_{23} \gamma + 4 T_{12} T_{23} + 2 (T_{23})^4 \gamma \\
& - (T_{23})^4 - 4 (T_{23})^2 \gamma^2 + 6 (T_{23})^2 + 4 \gamma^2 - 2 \gamma - 1 \Big)
\end{aligned}$$

with $T_{12} = T_{12}(\gamma)$ and $T_{23} = T_{23}(\gamma)$ given by eqns. 35 and 39, respectively.

The resulting angle $\theta_{TW}(\gamma)$ as a function of γ is plotted in fig. 6. The plot suggests that $\theta_{TW} \rightarrow +360^\circ$ as $\gamma \rightarrow \infty$. As already mentioned in subsection 4.3 (see fig. 2) the boost angles $\zeta_{1,2} \rightarrow +180^\circ$ and $\zeta_{2,3} \rightarrow +180^\circ$ in the relativistic limit $\gamma \rightarrow \infty$. Notwithstanding that the R 's trajectory reduces to an one-dimensional motion along the x -axis as $\gamma \rightarrow \infty$, the grid's Thomas-Wigner rotation angle approaches a full revolution of $+360^\circ$ in the laboratory frame.

6.2. Event horizons

As illustrated by fig. 5 the Born-rigid object \mathcal{G} rotates in the xy -plane. Clearly, \mathcal{G} 's spatial extent in the x - and y -directions has to be bounded by a maximum distance

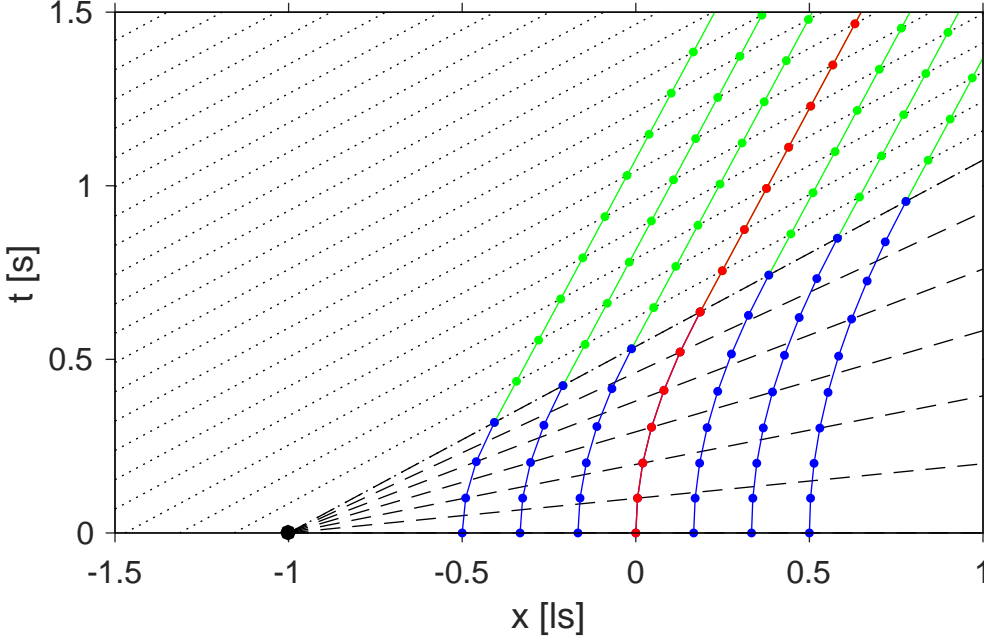


Figure 7. Spacetime diagram of a one-dimensional grid consisting of seven points. The grid accelerates towards the positive x -direction. The trajectories are marked in blue, the mid point is taken as the reference R and its worldline is colored in red. Dots indicate the lapse of 0.1 s in proper time. After 0.6 s have passed on R 's proper time close the acceleration stops and the points move with constant velocity (green lines). Dashed lines connect spacetime points of R 's comoving frame. The grey area indicates the inaccessible spacetime beyond the event horizon.

from the reference point R on the order of $\Delta t/\theta_{TW}$ [Born, 1909]. This boundary, which prevents paradoxical faster-than-light translations of sufficiently distant vertices, is produced by event horizons associated with the accelerations in the five boost sections.

Fig. 7 exemplifies the formation of an event horizon for an accelerated object in 1+1 (one time and one space) dimensions [see e.g. Desloge and Philpott, 1987; Eriksen et al., 1982; Hamilton, 1978; Semay, 2006]. Here, the Born-rigid object is assumed to be one-dimensional and to consist of seven equidistant grid points. Each point accelerates for a finite time period towards the positive x -direction (blue worldlines); the reference point R , marked in red, accelerates with $\alpha_R \equiv 1 \text{ ls/s}^2$. Contrary to the simulations discussed in fig. 5 above, in the present case the acceleration phase is not followed immediately by another boost. Rather, the object continues to move with constant velocity after the accelerating force has been switched off (green worldlines in fig. 7). The completion of the acceleration phase is synchronous in R 's instantaneous comoving frame (dashed-dotted line) and asynchronous in the laboratory frame. Fig. 7 also illustrates

that for an uniform acceleration the event horizon (black dot) is stationary with respect to the laboratory frame.

In this simulation each vertex is assumed to be equipped with an ideal clock ticking at a proper frequency of 10 Hz, the corresponding ticks are marked by dots; the boost phase lasts for 0.6 s on R 's clock. The clocks of the left-most (trailing) and right-most (leading) vertex measure (proper time) boost durations of 0.3 s and 0.9 s, respectively. Thus, with respect to the instantaneous comoving frames (dashed lines) the vertex clocks run at different rates (see eqn. 14). The trailing clocks tick slower, the leading clocks faster than the reference clock at R . From eqns. 13 and 14 it follows that the proper time variations are compensated by corresponding changes in proper acceleration experienced by the seven vertices. For the parameters used in fig. 7 the accelerations of the trailing and leading vertex are $2\alpha_R$ and $2\alpha_R/3$, respectively.

The spatial components of the inertial reference frames, comoving with R , are plotted in fig. 7 as well. During the acceleration-free period following the boost phase the grid moves with constant velocity and the equal-time slices of the corresponding comoving frames (dotted lines) are oriented parallel to other. During the boost phase, however, the lines intersect and eqn. 10 entails that the equal-time slices of the comoving frames all intersect in one spacetime point, the event horizon $x_H \equiv -1$ ls (black dot at $x = -1$ ls and $t = 0$ s in fig. 7). A clock placed at x_H does not tick, time is frozen at this spacetime point and eqns. 13 and 14 imply that the corresponding proper acceleration diverges. Clearly a physical object accelerating towards positive x in fig. 7 cannot extend beyond this boundary at x_H . If the grid in fig. 7 is regarded as realization of an accelerating coordinate system, this frame is bounded in the spatial dimension and ends at the coordinate value x_H . However, as soon as the grid's acceleration stops, the event horizon disappears and coordinates $x < x_H$ are permissible. We note, that the event horizon in fig. 7 is a zero-dimensional object, a point in $1 + 1$ -dimensional spacetime considered here. The horizon is frozen in time and exists only for the instant $t = 0$.

Generalizing this result we find that the five boosts described in subsection 4.3 and depicted in fig. 3 induce five event horizons in various orientations. It turns out that the accelerated object \mathcal{G} is bounded by these horizons in all directions within the xy -plane. They limit \mathcal{G} 's maximum size [Born, 1909] and thereby assure that all of its vertices obey the special relativistic speed limit [Einstein, 1905].

7. Conclusions

It is well known that pure Lorentz transformations do not form a group in the mathematical sense, since the composition of two transformations in general is not a pure Lorentz transformation again, but involves the Thomas-Wigner spatial rotation. The rotation is illustrated by uniformly accelerating a Born-rigid object, which is assumed to consist of a finite number of vertices, repeatedly, such that the object's reference point returns to its start location. It turns out that at least five boosts are necessary, provided, first, the (proper time) duration and the magnitude of the proper acceleration

within each boost is the same and, second, the object's motion is restricted to the xy -plane. Analytic expressions are derived for the angles between adjacent boost directions.

The visualizations illustrate the relationship between Thomas-Wigner rotations and the relativity of simultaneity. The transition from one boost section to the next occurs synchronously in the instantaneous comoving frame. In the laboratory frame, however, the trailing vertices conclude the current boost phase first and switch to the next one, which in general involves a direction change. In the laboratory frame the accelerated object not only contracts and expands along its direction of propagation, but also exhibits a shearing motion during the switchover phases. The simulations illustrate clearly that the aggregation of these shearing contributions finally adds up to the Thomas-Wigner rotation.

Accelerated motions induce event horizons, which no part of a physical, Born-rigid object may overstep. Thus, the object's size is limited to a finite volume or area (if its motion is restricted to two spatial dimension) and Thomas-Wigner rotations by construction observe the special relativistic speed limit.

8. Auxiliary material

An MPEG-4 movie showing the Thomas-Wigner rotation of a grid object is available at the URL www.gbeyerle.de/twr. In addition, the MATLAB source code used to create fig. 5 and the “SymPy” script file discussed in Appendix A can be downloaded from the same site.

Acknowledgments

Some calculations described in this paper were performed with the help of the computer algebra system “SymPy” [Joyner et al., 2012], which is available for download from www.sympy.org. “SymPy” is licensed under the General Public License; for more information see www.gnu.org/licenses/gpl.html. Trademarks are the property of their respective owners.

Appendix A.

A number of equations in this paper were derived using the computer algebra system “SymPy” [Joyner et al., 2012]. The corresponding “SymPy” source code files `vtwr3bst.py` (three boost case, see subsection 4.1) and `vtwr5bst.py` (five boost case, see subsection 4.3) are available for download at www.gbeyerle.de/twr. These scripts process eqns. 16, 17, 23 and 24 and derive the results given in eqns. 21, 22, 29, 31, 32, 44 and 45. The following offers a few explanatory comments.

First, we address the case of three boosts (“SymPy” script `vtwr3bst.py`) and the derivation of eqn. 21. The corresponding boost vectors in the xy -plane $\hat{e}_i^{(3B)}$ with

$i = 1, 2, 3$ are taken to be

$$\begin{aligned}\hat{e}_1^{(3B)} &\equiv \begin{pmatrix} C_a \\ S_a \end{pmatrix} = \frac{1}{1 + (T_{12})^2} \begin{pmatrix} 1 - (T_{12})^2 \\ 2 T_{12} \end{pmatrix} \\ \hat{e}_2^{(3B)} &\equiv \begin{pmatrix} 1 \\ 0 \end{pmatrix} \\ \hat{e}_3^{(3B)} &\equiv \begin{pmatrix} C_a \\ -S_a \end{pmatrix} = \frac{1}{1 + (T_{12})^2} \begin{pmatrix} 1 - (T_{12})^2 \\ -2 T_{12} \end{pmatrix}\end{aligned}\tag{A.1}$$

with

$$S_a \equiv \sin(\zeta_{1,2}) \quad C_a \equiv \cos(\zeta_{1,2})\tag{A.2}$$

in terms of the direction angle $\zeta_{1,2}$ and the half-angle approximation (eqn. 5). Here, the z -coordinate has been omitted since the trajectory is restricted to the xy -plane and $\zeta_{2,3} = \zeta_{1,2}$ from time reversal symmetry is being used. Inserting the corresponding Lorentz transformation matrices (eqn. 1) into eqn. 17 and selecting the time component yields

$$(\gamma - 1) \frac{((T_{12})^2 - 2\gamma - 1)^2}{((T_{12})^2 + 1)^2} = 0\tag{A.3}$$

which reduces to eqn. 21 if the trivial solution $\gamma = 1$ is ignored.

The case of five boosts (“SymPy” script `vtwr5bst.py`) and the derivation of eqn. 31 is addressed next. In analogy to eqn. A.1 we define

$$\begin{aligned}\hat{e}_1^{(5B)} &\equiv \begin{pmatrix} C_x \\ S_x \end{pmatrix} = \begin{pmatrix} C_{12} C_{23} - S_{12} S_{23} \\ -S_{12} C_{23} - C_{12} S_{23} \end{pmatrix} \\ \hat{e}_2^{(5B)} &\equiv \begin{pmatrix} C_y \\ S_y \end{pmatrix} = \begin{pmatrix} C_{23} \\ -S_{23} \end{pmatrix} = \frac{1}{1 + (T_{23})^2} \begin{pmatrix} 1 - (T_{23})^2 \\ -2 T_{23} \end{pmatrix} \\ \hat{e}_3^{(5B)} &\equiv \begin{pmatrix} 1 \\ 0 \end{pmatrix} \\ \hat{e}_4^{(5B)} &\equiv \begin{pmatrix} C_y \\ -S_y \end{pmatrix} = \begin{pmatrix} C_{23} \\ S_{23} \end{pmatrix} = \frac{1}{1 + (T_{23})^2} \begin{pmatrix} 1 - (T_{23})^2 \\ 2 T_{23} \end{pmatrix} \\ \hat{e}_5^{(5B)} &\equiv \begin{pmatrix} C_x \\ -S_x \end{pmatrix} = \begin{pmatrix} C_{12} C_{23} - S_{12} S_{23} \\ S_{12} C_{23} + C_{12} S_{23} \end{pmatrix}\end{aligned}\tag{A.4}$$

with eqn. A.2 and

$$\begin{aligned}S_{12} &\equiv \sin(\zeta_{1,2}) & C_{12} &\equiv \cos(\zeta_{1,2}) \\ S_{23} &\equiv \sin(\zeta_{2,3}) & C_{23} &\equiv \cos(\zeta_{2,3})\end{aligned}\tag{A.5}$$

The corresponding Lorentz transformation matrices are too unwieldy to reproduce them here. “SymPy” script `vtwr5bst.py` calculates them, their products in terms of T_{12} and

T_{23} and inserts them into eqn. 24. Selecting the time component yields the equation

$$\begin{aligned} & \frac{\gamma - 1}{((T_{12})^2 + 1)^2 ((T_{23})^2 + 1)^2} \\ & \times ((T_{12})^2 (T_{23})^2 + (T_{12})^2 - 4 T_{12} T_{23} \gamma \\ & - 4 T_{12} T_{23} - 2 (T_{23})^2 \gamma - (T_{23})^2 + 4 \gamma^2 + 2 \gamma - 1)^2 = 0 \quad . \end{aligned} \quad (\text{A.6})$$

We exclude the trivial solution $\gamma = 1$ and restrict ourselves to real values of T_{12} and T_{23} ; eqn. A.6 then leads to eqn. 28, a second order polynomial with respect to T_{23} . The two solutions are given in eqn. 29.

Next insert $T_{23} = T_{23}(T_{12}, \gamma)$ in eqn. 23. Since its time component involves the travel time of R along its closed trajectory as an additional unknown and the z -coordinate vanishes by construction, we focus in the following on the x - and y -components of eqn. 23. The script `vtwr5bst.py` shows that the result for the y -component of the four-vector equation $\vec{P}_F^{[6]} = 0$ can be expressed in the form

$$-8 ((T_{12})^2 + 1) (\gamma + 1)^2 \frac{X_1(T_{12}, \gamma) + X_2(T_{12}, \gamma) \sqrt{X_3(T_{12}, \gamma)}}{((T_{12})^2 - 2\gamma - 1)^6} = 0 \quad (\text{A.7})$$

Here, $X_i(T_{12}, \gamma)$ with $i = 1, 2, 3$ are polynomials in T_{12} .

For real T_{12} and $\gamma \geq 1$ the numerator has to equate to zero. Moving the term involving the square root to the RHS and squaring both sides yields

$$(X_1(T_{12}, \gamma))^2 - (X_2(T_{12}, \gamma))^2 X_3(T_{12}, \gamma) = 0 \quad . \quad (\text{A.8})$$

Evaluation of this expression (see script `vtwr5bst.py`) leads to the product of two polynomial expression, each of which is fourth order with respect to $(T_{12})^2$ (see eqn. 31 and 32).

Repeating these calculations for the x -component of the four-vector equation $\vec{P}_F^{[6]} = 0$ leads also to the product of two polynomial expression, one of which is identical to eqn. 31. Thus, we have found a solution to eqn. 25.

The Thomas-Wigner angle θ_{TW} (eqn. 43) follows from the Lorentz matrix relating frame [1] to frame [6] (eqn. 41). Script `vtwr5bst.py` evaluates the matrix elements $R_{1,1}$ and $R_{2,1}$ in terms of the variable T_{12} and T_{23} . Again the expressions are unwieldy, but the derivation is straightforward.

References

- J. S. Bell. *Speakable and Unspeakable in Quantum Mechanics*. Cambridge University Press, Cambridge, second edition, 2004. ISBN 978-0-521-52338-7.
- A. Ben-Menahem. Wigners rotation revisited. *Am. J. Phys.*, 53(1):62–66, 1985. doi:10.1119/1.13953.
- M. Born. Die Theorie des starren Elektrons in der Kinematik des Relativitätsprinzips. *Annalen der Physik*, 335(11):1–56, 1909. doi:10.1002/andp.19093351102.
- J. P. Costella, B. H. J. McKellar, A. A. Rawlinson, and G. J. Stephenson Jr. The Thomas rotation. *Am. J. Phys.*, 69(8):837–847, 2001. doi:10.1119/1.1371010.

- J. T. Cushing. Vector Lorentz transformations. *Am. J. Phys.*, 35(9):858–862, 1967. doi:10.1119/1.1974267.
- E. A. Desloge and R. J. Philpott. Uniformly accelerated reference frames in special relativity. *Am. J. Phys.*, 55(3):252–261, 1987. doi:10.1119/1.15197.
- E. Dewan and M. Beran. Note on stress effects due to relativistic contraction. *Am. J. Phys.*, 27(7):517–518, 1959. doi:10.1119/1.1996214.
- E. M. Dewan. Stress effects due to Lorentz contraction. *Am. J. Phys.*, 31(5):383–386, 1963. doi:10.1119/1.1969514.
- A. Einstein. Zur Elektrodynamik bewegter Körper. *Annalen der Physik*, 322(10):891–921, 1905. doi:10.1002/andp.19053221004.
- E. Eriksen, M. Mehlen, and J. M. Leinaas. Relativistic rigid motion in one dimension. *Phys. Scr.*, 25(6B):905–910, 1982. doi:10.1119/1.1996214.
- A. A. Evett. A relativistic rocket discussion problem. *Am. J. Phys.*, 40(8):1170–1171, 1972. doi:10.1119/1.1986781.
- A. A. Evett and R. K. Wangsness. Note on the separation of relativistically moving rockets. *Am. J. Phys.*, 28(6):566–566, 1960. doi:10.1119/1.1935893.
- F. Fernflores. Bell’s spaceships problem and the foundations of special relativity. *Int. Stud. Philos. Sci.*, 25(4):351–370, 2011. doi:10.1080/02698595.2011.623364.
- R. Ferraro and M. Thibeault. Generic composition of boosts: an elementary derivation of the Wigner rotation. *Eur. J. Phys.*, 20(3):143–151, 1999. doi:10.1088/0143-0807/20/3/003.
- G. P. Fisher. The Thomas precession. *Am. J. Phys.*, 40(12):1772–1781, 1972. doi:10.1119/1.1987061.
- J. Franklin. Lorentz contraction, Bell’s spaceships and rigid body motion in special relativity. *Eur. J. Phys.*, 31(2):291–298, 2010. doi:10.1088/0143-0807/31/2/006.
- H. Gelman. Sequences of co-moving Lorentz frames. *J. Math. Anal. Appl.*, 145(2):524–538, 1990. doi:10.1016/0022-247X(90)90418-F.
- E. Gourgoulhon. *Special Relativity in General Frames*. Springer, Berlin, Heidelberg, 2013.
- J. D. Hamilton. The uniformly accelerated reference frame. *Am. J. Phys.*, 46(1):83–89, 1978. doi:10.1119/1.11169.
- G. Herglotz. Über den vom Standpunkt des Relativitätsprinzips aus als starr zu bezeichnenden Körper. *Annalen der Physik*, 336(2):393–415, 1909. doi:10.1002/andp.19103360208.
- M. P. Hobson, G. P. Efstathiou, and A. N. Lasenby. *General relativity: An introduction for physicists*. Cambridge University Press, Cambridge, 2006. ISBN 0-521-82951-8.
- R. M. Jonsson. Gyroscope precession in special and general relativity from basic principles. *Am. J. Phys.*, 75(5):463–471, 2007. doi:10.1119/1.2719202.

- D. Joyner, O. Čertík, A. Meurer, and B. E. Granger. Open source computer algebra systems: SymPy. *ACM Communications in Computer Algebra*, 45(3/4):225–234, 2012. doi:10.1145/2110170.2110185.
- W. L. Kennedy. Thomas rotation: A Lorentz matrix approach. *Eur. J. Phys.*, 23(3): 235–247, 2002. doi:10.1088/0143-0807/23/3/301.
- C. W. Misner, K. S. Thorne, and J. A. Wheeler. *Gravitation*. Palgrave Macmillan, 1973. ISBN 978-0716703440.
- C. I. Mocanu. On the relativistic velocity composition paradox and the Thomas rotation. *Found. Phys. Lett.*, 5(5):443–456, 1992. doi:10.1007/BF00690425.
- F. Noether. Zur Kinematik des starren Körpers in der Relativtheorie. *Annalen der Physik*, 336(5):919–944, 1910. doi:10.1002/andp.19103360504.
- K. Rebilas. Subtleties of the Thomas precession. *Eur. J. Phys.*, 36(4):1–13, 2015. doi:10.1088/0143-0807/36/4/045007.
- D. V. Redžić. Note on Dewan–Beran–Bell’s spaceship problem. *Eur. J. Phys.*, 29(3): N11–N19, 2008. doi:10.1088/0143-0807/29/3/N02.
- J. A. Rhodes and M. D. Semon. Relativistic velocity space, Wigner rotation, and Thomas precession. *Am. J. Phys.*, 72(7):943–960, 2004. doi:10.1119/1.1652040.
- W. Rindler. *Relativity: Special, General, and Cosmological*. Oxford University Press, USA, 2006.
- E. G. P. Rowe. The Thomas precession. *Eur. J. Phys.*, 5(1):40–45, 1984. doi:10.1088/0143-0807/5/1/009.
- C. Semay. Observer with a constant proper acceleration. *Eur. J. Phys.*, 27(5):1157–1167, 2006. doi:10.1088/0143-0807/27/5/015.
- A. M. Steane. *Relativity Made Relatively Easy*. Oxford University Press, 2012. ISBN 019966286X.
- D. F. Styer. How do two moving clocks fall out of sync? A tale of trucks, threads, and twins. *Am. J. Phys.*, 75(9):805–814, 2007. doi:10.1119/1.2733691.
- A. Tartaglia and M. L. Ruggiero. Lorentz contraction and accelerated systems. *Eur. J. Phys.*, 24(2):215–220, 2003. doi:10.1088/0143-0807/24/2/361.
- L. H. Thomas. The motion of the spinning electron. *Nature*, 117(2945):514–514, 1926. doi:10.1038/117514a0.
- L. H. Thomas. The kinematics of an electron with an axis. *Philos. Mag.*, 3(13):1–22, 1927. doi:10.1080/14786440108564170.
- S.-I. Tomonaga. *The story of spin*. The University of Chicago Press, Chicago, 1997. ISBN 0-226-80794-0.
- A. A. Ungar. The relativistic velocity composition paradox and the Thomas rotation. *Found. Phys.*, 19(11):1385–1396, 1989. doi:10.1007/BF00732759.

- A. A. Ungar. Thomas precession: Its underlying gyrogroup axioms and their use in hyperbolic geometry and relativistic physics. *Found. Phys.*, 27(6):881–951, 1997. doi:10.1007/BF02550347.
- E. P. Wigner. On unitary representations of the inhomogeneous Lorentz group. *Ann. Math.*, 40(1):149–204, 1939. doi:10.2307/1968551.